International Journal of Greenhouse Gas Control 90 (2019) 102800

Contents lists available at ScienceDirect

International Journal of Greenhouse Gas Control

journal homepage: www.elsevier.com/locate/ijggc

CPFD simulation and optimization of a 50 kW_{th} dual circulating fluidized bed reactor for chemical looping combustion of coal

Xi Chen, Jinchen Ma, Xin Tian, Jianlong Wan, Haibo Zhao*

State Key Laboratory of Coal Combustion, School of Energy and Power Engineering, Huazhong University of Science and Technology, Wuhan 430074, China

ARTICLE INFO

Keywords:
Chemical looping
CPFD simulation
Gas-solid reactive flow
Operation optimization

ABSTRACT

A 50 kW_{th} dual circulating fluidized bed reactor for chemical looping combustion (CLC) of coal, which has been designed, constructed and operated at Huazhong University of Science & Technology (HUST), was simulated using the Computational Particle Fluid Dynamics (CPFD) method in this work. The reliability of CPFD simulation was first validated by comparing fuel reactor (FR) outlet gases concentration and FR pressure profiles of experimental measurements with the corresponding simulation results. Then, the gas-solid reactive flow in the full-scale reactor was simulated in detail, and the results can help to rationalize reactor design and optimize operation. The evolution of bed inventory and solid circulation rate were carefully analyzed to understand the bed material rebalance phenomenon observed in simulation. The self-adjustment ability among different parts within the whole unit demonstrated the feasibility and stability of the 50 kW_{th} CLC reactor. In addition, to have a better understanding on the relationships among the complex factors of hydrodynamics and reactions, the residence time distributions of oxygen carrier (OC) and char were attained. Based on these results, a higher FR was proposed as an optimization to improve the residence time of char in FR, so as to extend reaction path of both homogeneous and heterogeneous reactions therein. Finally, according to the simulation results of the combustible gases distribution and coal conversion trail within the reactor, the coal feeding location was optimized. It was found that the combustible gases in volatile plume cannot diffuse effectively throughout FR with only one coal feeding point, which was not conductive to the good mixing among OC and combustible gases. As an optimization, well mixed gas-solid contact was achieved with two oppositely-collocated coal feeding points. In summary, the CPFD simulation conducted in this work can help to optimize the reactor configuration and operation, which eventually achieved reliable prediction of the performance of the 50 kW_{th} CLC reactor in an effective and economical way.

1. Introduction

It is believed that the increasing emission of CO_2 may become a serious challenge to all aspects of human civilization. While the utilization of fossil fuels has been considered as the biggest contributor to CO_2 emission, fossil fuels are still going to be the dominant energy in the foreseeable future (Hamilton et al., 2016). Therefore, it is of urgent need to come up with greener ways for fossil fuel conversion (Metz et al., 2005). Chemical looping combustion (CLC), which has the feature of CO_2 inherent separation, is considered as a promising way for low-carbon fossil fuel utilization (Fan and Li, 2010; Zhao et al., 2008). A typical CLC system consists of two structurally-interconnected but atmosphere-isolated fluidized bed reactors: an air reactor (AR) and a fuel reactor (FR). A kind of solid intermediate, a.k.a. oxygen carrier (OC), circulates between AR and FR, connecting the two reactors in both thermal and chemical ways. In the FR, the fuel is oxidized by the lattice oxygen in OC with high oxygen potential (M_xO_y), and the resulting gaseous products are theoretically only CO_2 and H_2O, which can be reused as the fluidization agent in FR (Lyngfelt et al., 2001). Also, high purity CO_2 stream can be captured at a lower cost from the flue gas of FR. Subsequently, the reduced OC (M_xO_{y-1}) circulates back to the AR and is re-oxidized by air to recuperate its oxygen capacity, so as to form a loop.

During the past decades, researches on chemical looping mainly focused on the selection and optimization of OC, gas-solid heterogeneous reaction kinetics, as well as the design, operation and simulation of CLC reactors (Adanez et al., 2012; Nandy et al., 2016). CLC facilities with thermal power ranging from 0.3 kW_{th} to 3 MW_{th} (Ma et al., 2018; Lyngfelt and Leckner, 2015) have been established by different research groups worldwide. Currently, most of the CLC

* Corresponding author.
E-mail address: hzhao@mail.hust.edu.cn (H. Zhao).

https://doi.org/10.1016/j.ijggc.2019.102800
Received 13 February 2019; Received in revised form 18 July 2019; Accepted 28 July 2019

Nomenclature

A	Surface area (m^2)
A_i	Pre-exponential factor (1/s)
c	Specific heat (J/kg K)
C_d	Drag coefficient
C_{coal}	Concentration of coal (kg/m^3)
d	Diameter (m)
E	Activation energy (kJ/mol)
f_h	Heat transfer ratio
$\boldsymbol{F}$	Force source (N)
F_D	Particle drag coefficient
$\boldsymbol{g}$	Gravity (m/s^2)
h	Heat transfer coefficient (J/m^2 K)
H	Enthalpy (J)
H_{reac}	Enthalpy changes (J/kg)
$\boldsymbol{J}$	diffusion flux (kg/m^2)
k	chemical reaction rate constant (mol^{1-n}/m^{2-3n} s)
m	Particle mass (kg)
MW	Molecular weight (kg/mol)
n	Reactor order
p	Pressure (Pa)
Q	Heat of reaction (J)
r	Reaction rate (mol/m^3 s)
R	Constant of the ideal gases (J/mol K)
Re	Reynolds number
S	Mass source (kg)
T	Temperature (K)
$\boldsymbol{u}$	Velocity vector (m/s)
X	Conversion rate
Y	Mass fraction
[·]	Concentration (mol/m^3)

Greek letters

α	Volume fraction
ε	Dissipation rate of turbulent kinetic energy (m^{-2} s^{-3})
λ	Thermal conductivity (W/m^2 K)
ρ	Density (kg/m^3)
$\boldsymbol{\tau}$	Stress-strain tensor (Pa)
μ	Viscosity (kg/m s)

Subscripts

g	Gas phase
gs	From particle phase to gas phase
i	Specie index
s	Particle phase

reactors are usually operated as retrofitted circulating fluidized bed mode, due to the flexible adjustability of solid circulation rate between AR and FR and the sufficient gas-solid contact (Linderholm et al., 2008). However, unconverted fuel gas and char are usually entrained out of FR. Therefore, operation optimization of such a complex gas-solid system is still required (Lyngfelt and Leckner, 2015). In addition, for the scale-up of the CLC unit, rational design of the CLC reactor is challenging as well. Computational fluid dynamics (CFD) simulation is an effective tool to understand the complex gas-solid reactive flow in a CLC unit, which can help to rationalize the design and operation of the CLC reactor with less cost in comparison with the experimental methodology. Three kinds of CFD models, *i.e.*, the two-fluid model (Deng et al., 2008; Wang et al., 2011), the CFD-DEM (discrete element method) model (Tabib et al., 2013; Zhang et al., 2014), and the CPFD (computational particle fluid dynamics) model, have been adopted in CLC simulations. Generally speaking, the two-fluid model and CPFD model are at the advantage of less computational cost than the CFD-DEM model, and thus being more widely used.

Extensive studies on CFD simulation have been conducted by many researchers to investigate the complicated hydrodynamics in CLC. And these investigations mainly focused on the development and application of available gas-solid reaction kinetics (Deng et al., 2009; Jung and Gamwo, 2008), reasonable heterogeneous models for gas-solid interaction (Wang et al., 2014; Su and Zhao, 2016), and appropriate hydrodynamics in reactor (Shao et al., 2017). For the application of the two-fluid model, which solves equations in the Eulerian-Eulerian way, the reliability of CFD simulation can be guaranteed by reasonable models. Mahalatkar et al. (2011a,b,c) carried out a series of investigations on CLC, developing models for the single FR, likewise the complete CLC system with two-fluid model based on the experiments of Leion et al. (2008), Son and Kim (2006), Abad et al. (2006), and Mattisson et al. (2001). Simulation results from these investigations, like outlet flue gas concentrations and solid mass distribution, agreed well with the experimental measurements, demonstrating that CFD simulation was an effective method to study the chemical and hydrodynamic influencing elements involving in CLC process. Su et al. (2015) simulated a 5 kW_{th} coal-fueled CLC reactor developed by our group in two dimensions, which accorded with experiments in a preferable way, bringing computation cost and veracity into balance. Flow pattern of gas and solid phase, gas leakage process between AR and FR, as well as reactor performance were simulated particularly to research the performance of the reactor. The trail of coal devolatilization and char gasification were also attainable for a comprehensive understanding about the unit. Based on the characteristic of this reactor, operating parameters including temperature and coal feeding amount were adjusted to achieve optimal state.

CPFD model, which is a kind of Eulerian-Lagrangian method, plays a remarkable role in numerical simulation of gas-solid reactive flow. Previously, the Eulerian-Eulerian method was thought to be superior over the Eulerian-Lagrangian method in some aspects, like computation cost (Guan et al., 2014). But recently, CPFD model gains more advantage over the two-fluid model in the simulation of massive and complicated gas-solid system in high concentration, being widely adopted not only in academic research but also in industry application. The CPFD method was developed by Andrews, O'Rourke (1996) and Snider (2001), and it can solve fluid and particle equations in three dimensions. In this methodology, the fluid equations are solved in the Eulerian approach on the mesh while the particles equations are solved in the Lagrangian manner with the implementation of the multiphase particle-in-cell (MP-PIC). Besides, the computational parcel, which is a group of particles with the same properties, is introduced to simplify the large-scale particle system simulation. However, the works employing CPFD of CLC reactor are quite few to date. Breault and Monazam (2016), Breault et al. (2017) presented a particle model which can describe the Johnson-Mehl-Avrami (JMA) kinetics with CPFD method. The simulation results were verified with the experimental data. This model was suitable for the Barracuda™, which is the typical code of CPFD and it was further used to simulate the FR of the NETL's 50 kW_{th} CLC reactor. Parker (2014) simulated a full-scale CLC system from NETL with Fe-based material as OC, trying to investigate the multiple heterogeneous and homogeneous reactions in CLC, as well as the heat transfer between AR and FR. The moisture release and swelling effects of coal particle during devolatilization were also considered and this attractive work further improved the accuracy of CLC simulation.

In recent years, our group have designed and constructed a 50 kW_{th} CLC unit. Experiments with bituminous coal as fuel and natural hematite as OC have been performed to test the behavior of the reactor at

different operational parameters, like the reaction temperature, FR inlet gas velocity, and gasification agent concentration (Ma et al., 2018). Proper control schemes for regulation and optimization of the CLC unit were determined by evaluating various indicators like combustion efficiency, CO_2 yield and carbon capture efficiency. According to these macroscopical and immediate targets, a systematic acquaintance of this unit was achieved. Nevertheless, there are also plenty of things, including solid circulation rate, bed inventory and residence time of particles that are difficult or impossible to be experimentally measured. And details of the gas-solid reactive flow in the reactor, like pressure, solid and gas distribution, are also crucial but not easy to access to. Therefore, in this study, a comprehensive CPFD simulation model was developed in three-dimensional of dual circulating fluidized bed reactor to have a better understanding on the coal-fueled CLC process. Several aspects, including gas-solid flow pattern, bed inventory and solid circulation self-adjustment, pressure balance and gas isolation of loop seal, residence time of char and OC particles in FR, trail of coal pyrolysis and char gasification were predicted, respectively. Based on the optimization of char residence time and coal feeding mode, better performance of the 50 kW_{th} unit was achieved.

2. CPFD model

The governing equations of fluid and particle are listed in Table 1, as summarized from the work of Snider et al. (2011). And the Gidaspow model was chosen as the drag model in the simulation.

During the continuous operation of the 50 kW_{th} coal-fueled CLC unit, natural hematite was used as OC and steam was adopted as the gasification agent. Coal particles fed into the FR were firstly devolatilized to generate volatiles, moisture, coal char, and ash, but some H_2O will be consumed if the gasification agent is steam (R1). As the operation was conducted in the temperature range of 900–1000 °C, the coal devolatilization process occurred quickly. Then the coal char will be gasified by CO_2/H_2O to produce CO and H_2 as R2 and R3. In the meanwhile, volatiles and gasification products (mainly CH_4, CO, and H_2) reacted with OC (R4-R6) and the active component (Fe_2O_3) in OC was partially reduced to Fe_3O_4 because of the high oxygen to fuel ratio in the tests. In the AR, the OC oxidation reaction (R7) and the residual char combustion reaction (R8) happened. Moreover, the water-gas shift reaction (R9) in FR was also considered in the simulation. The reaction kinetics used in this work are summarized in Table 2. These models were obtained from sources in open literatures. The coal devolatilization chemistry was chosen from Su et al. (2015) and Wang et al. (2013), and the unit of R1 is g or kg. The reaction rate expression, in which forward direction and reverse direction were combined as one equation, *i.e.*, char gasification and water-gas shift reaction, were from Snider et al. (2011), and these kinetics were primarily obtained by Syamlal and Bissett (1992) and Bustamante et al. (2004, 2005). The heterogeneous reaction models between combustible gases and OC were from the works of Mahalatkar et al. (2011c) and Su et al. (2015), and the kinetic parameters adopted for these reactions came from Abad et al. (2007).

3. Reactor structure, initial conditions and boundary conditions

A schematic view of the 50 kW_{th} CLC reactor simulated in this work is shown in Fig. 1. The dimension of the simulation model is the same as the actual one. The reactor consists of an air reactor (AR), a fuel reactor (FR), as well as the connection components, *i.e.*, risers, down comers, loop seals and cyclones. A carbon stripper is incorporated in the loop seal of FR, but it was operated for reaction instead of physical separation in the previous experiment and simulation. The dimension of AR, FR, and risers can be seen in Fig. 1 and the pressure detection points are presented as dots marked with numbers from 1 to 40. The distance between adjacent pressure detection points in AR and FR is 0.1 m, while it is 0.5 m in the riser. Note that, the distribution of pressure detection points adopted in simulation in Fig. 1 is more intensive than that in experiment. There are two places for coal-feeding: one is the coal feeding pipe which is used in all cases of simulation, and the other one is the opposite-collocated coal feeding points. In this work, the CPFD model simulated multiple sizes and types of particles and disparate fluidization regimes simultaneously, including bubbling fluidized bed in FR, turbulent fluidized bed in AR, particle transportation in riser, moving bed in loop seal, and particle-fluid separation in cyclone. Corresponding to the presence of these processes, particle concentration ranging from closely-packed to extremely dilute existed in the same model. Besides, the use of coal in the simulation also introduced additional complexities because of the complicated composition and reactions involved.

Natural hematite was used as OC in both experiment and simulation. The hematite OC was in the diameter range of 150–350 μm, and the particle density was 3650 kg/m^3. The chemical composition of the hematite is shown in Table 3. Shenhua bituminous coal from China was used as fuel in this work. The coal particles ranged from 100 μm to 300 μm, and the proximate and ultimate analysis are shown in Table 4. Initial conditions and boundary conditions are summarized in Table 5. It should be noted that the recycle chamber is the chamber in loop seal connecting with AR or FR, while the supply chamber is the one connecting with AR down comer or FR down comer, like Fig. 1. The initial bed inventory in simulations was based on the results obtained in experiment after a period of time of operation which was not the initial value but the one during the OC redistribution of dynamic balance and this setting reduced the simulation time to reach a balance but put no influence on the results because the final bed inventory distribution was determined once the operation parameters were confirmed. Moreover, the heat needed in this unit was supplied by the help of an electric heater. The heat transfer coefficient between gas phase and solid phase was taken into consideration in this work, as well as the heat transfer between gas and reactor wall. It is worth noting, however, that the reaction heat was quite small in comparison to that from the electrical heater.

Before conducting the detailed simulation, a pre-calculation was carried out to determine the appropriate cell number, particle resolution and time step. The exhaust concentration and pressure profiles of

Table 1
Governing equations of CPFD.

Mass conservation,

$$\frac{\partial}{\partial t}(\alpha\rho)_g + \nabla\cdot(\alpha\rho\mathbf{u})_g = S_{gs}$$

Species mass conversion,

$$\frac{\partial}{\partial t}(\rho\alpha Y_i)_g + \nabla(\rho\alpha\mathbf{u}Y_i)_g = -\nabla\alpha_g\mathbf{J}_{g,i} + \alpha_g S_{gs,i}$$

Momentum conservation,

$$\frac{\partial}{\partial t}(\alpha\rho\mathbf{u})_g + \nabla\cdot(\alpha\rho\mathbf{u}^2)_g = -\alpha_g\nabla p + \alpha_g\rho_g\mathbf{g} + \nabla\cdot\tau_g - \beta_{DPM}(\mathbf{u}_g - \mathbf{u}_s) + S_{gs}\mathbf{u}_g$$

$$\beta_{DPM} = \begin{cases} 150\frac{(1-\alpha_g)^2\mu_g}{\alpha_g d_s^2} + 1.75\frac{\rho_g\alpha_s\,|\,\mathbf{u}_g-\mathbf{u}_s|}{d_s} & (\alpha_g \le 0.8) \\ \frac{3}{4}C_d\frac{\alpha_g^{-1.65}\alpha_s\rho_g\,|\,\mathbf{u}_g-\mathbf{u}_s|}{d_s} & (\alpha_g > 0.8) \end{cases}$$

$$C_d = \begin{cases} \frac{24}{\alpha_g \mathrm{Re}}[1 + 0.15(\alpha_g\,\mathrm{Re})^{0.687}] & (\mathrm{Re}\le 1000) \\ 0.44 & (\mathrm{Re} > 1000) \end{cases}$$

$$\mathrm{Re} = \frac{|\mathbf{u}_g - \mathbf{u}_s|\,\rho_g d_s}{\mu_g}$$

Energy equation,

$$\frac{\partial}{\partial t}(\alpha\rho H)_g + \nabla(\alpha\rho\mathbf{u}H)_g = \alpha_g\nabla(\lambda_g\nabla T_g) + Q_{gs} + S_{gs}H_g$$

Particle velocity,

$$\frac{d\mathbf{u}_s}{dt} = F_D(\mathbf{u} - \mathbf{u}_s) + \frac{\mathbf{g}(\rho_s - \rho)}{\rho_s} + \mathbf{F} - \frac{1}{\rho_s}\nabla\cdot\tau_s$$

$$\tau_s = \frac{10P_s\alpha_s^{\beta}}{\max[\alpha_{cs} - \alpha_s, \varepsilon(1-\alpha_s)]}$$

Particle temperature,

$$m_s c_s\frac{dT_s}{dt} = hA_s(T_\infty - T_s) - f_h\frac{dm_s}{dt}H_{reac}$$

Table 2
Reactions and the reactive kinetics models.

Reaction	Chemistry equation and reaction rate
R1	Coal+0.001748H_2O→ 0.4846Char+0.09427CO+0.03989CO_2+0.02236CH_4+0.01723H_2 +0.3434Ash $r_{pyroly} = (Y_a k_a + Y_b k_b) C_{coal}$, $k_i = A_i \exp(-E_i/RT_s)$, $A_a = 2 \times 10^5 s^{-1}$, $A_b = 1.3 \times 10^7 s^{-1}$, $E_a = 104.6 kJ \cdot mol^{-1}$, $E_b = 167.4 kJ \cdot mol^{-1}$, $Y_a = 0.3$, $Y_b = 1.0$
R2	Char+CO_2 ↔ 2CO $r_2 = 1.272 m_s T \exp(-22645/T)[CO_2] - 1.044 \times 10^{-4} m_s T^2 \exp(-2263/T - 20.92)[CO]^2$
R3	Char+H_2O↔ CO+H_2 $r_2 = 1.272 m_s T \exp(-22645/T)[H_2O] - 1.044 \times 10^{-4} m_s T^2 \exp(-6319/T - 17.29)[H_2][CO]$
R4	CH_4+12Fe_2O_3 → 8Fe_3O_4+2H_2O+CO_2 $\dot{m}_{CH_4} = \frac{k_{CH_4} R_0}{2MW_{O_2}} \rho_s \varepsilon_s (Y_{Fe_2O_3} + Y_{Fe_3O_4} \times \frac{S_{Fe_2O_3} M_{Fe_2O_3}}{S_{Fe_3O_4} M_{Fe_3O_4}})(1-X)^{\frac{2}{3}} MW_{CH_4}$, $k_{CH_4} = \frac{3bk_0 e^{-E/RT}}{\rho_m r_0} C^n_{CH_4}$, $\rho_m = 60627 mol \cdot m^{-3}$, $r_0 = 3.29 \times 10^{-7} m$, $b = 12$, $k_0 = 8.0 \times 10^{-4}$, $E = 49 kJ \cdot mol^{-1}$, $n = 1.3$
R5	CO+3Fe_2O_3 → 2Fe_3O_4+CO_2 $\dot{m}_{CO} = \frac{2k_{CO} R_0}{MW_{O_2}} \rho_s \varepsilon_s (Y_{Fe_2O_3} + Y_{Fe_3O_4} \times \frac{S_{Fe_2O_3} M_{Fe_2O_3}}{S_{Fe_3O_4} M_{Fe_3O_4}})(1-X)^{\frac{2}{3}} MW_{CO}$, $k_{CO} = \frac{3bk_0 e^{-E/RT}}{\rho_m r_0} C^n_{CO}$, $\rho_m = 60627 mol \cdot m^{-3}$, $r_0 = 3.29 \times 10^{-7} m$, $b = 3$, $k_0 = 6.2 \times 10^{-4}$, $E = 20 kJ \cdot mol^{-1}$, $n = 1.0$
R6	H_2+3Fe_2O_3 → 2Fe_3O_4 + H_2O $\dot{m}_{H_2} = \frac{2k_{H_2} R_0}{MW_{O_2}} \rho_s \varepsilon_s (Y_{Fe_2O_3} + Y_{Fe_3O_4} \times \frac{S_{Fe_2O_3} M_{Fe_2O_3}}{S_{Fe_3O_4} M_{Fe_3O_4}})(1-X)^{\frac{2}{3}} MW_{H_2}$, $k_{H_2} = \frac{3bk_0 e^{-E/RT}}{\rho_m r_0} C^n_{H_2}$, $\rho_m = 60627 mol \cdot m^{-3}$, $r_0 = 3.29 \times 10^{-7} m$, $b = 3$, $k_0 = 2.3 \times 10^{-3}$, $E = 24 kJ \cdot mol^{-1}$, $n = 0.8$
R7	4Fe_3O_4 + O_2 → 6Fe_2O_3 $\dot{m}_{O_2} = \frac{k_{O_2} R_0}{MW_{O_2}} \rho_s \varepsilon_s (Y_{Fe_2O_3} + Y_{Fe_3O_4} \times \frac{S_{Fe_2O_3} M_{Fe_2O_3}}{S_{Fe_3O_4} M_{Fe_3O_4}}) X^{\frac{2}{3}} MW_{O_2}$, $k_{O_2} = \frac{bk_0 e^{-E/RT}}{\rho_m r_0} C^n_{O_2}$, $\rho_m = 41523 mol \cdot m^{-3}$, $r_0 = 1.8 \times 10^{-7} m$, $b = 4$, $k_0 = 3.1 \times 10^{-4}$, $E = 14 kJ \cdot mol^{-1}$, $n = 1.0$
R8	Char+O_2 → CO_2
R9	CO+H_2O↔ CO_2 + H_2 $r_9 = 7.68 \times 10^{10} \exp(-36640/T)[CO]^{0.5}[H_2O] - 6.4 \times 10^9 \exp(-39260/T)[H_2]^{0.5}[CO_2]$

FR were monitored at different cell number and particle resolution conditions for examination. Finally, the results indicated good grid and resolution independence and fitness at the cell number of 476,000 with 2,139,908 particles. The Cartesian mesh was adopted in the simulation and the time step was 0.00001 s after self-fitness with GPU parallel computing.

4. Results and discussion

4.1. Validation of the simulation models

At the beginning, the computational model of the 50 kW_{th} coal-fueled CLC reactor was validated by comparing the simulation results of FR flue gas concentrations and pressure distribution in the axis of FR with experimental one. Table 6 shows the detailed comparison of the gas volume fraction in FR exhaust detected in simulation and experiment under different operational conditions, *i.e.*, reaction temperature, concentration of gasification agent and superficial velocity of FR, in which case 2 is the working condition in the following parts of this paper and others are for validation. It should be noted that the exhaust

Table 3
Chemical analysis of the hematite used in experiment and simulation.

Composition	Fe_2O_3	SiO_2	CaO	Others
wt.%	90.09	3.41	5.33	1.17

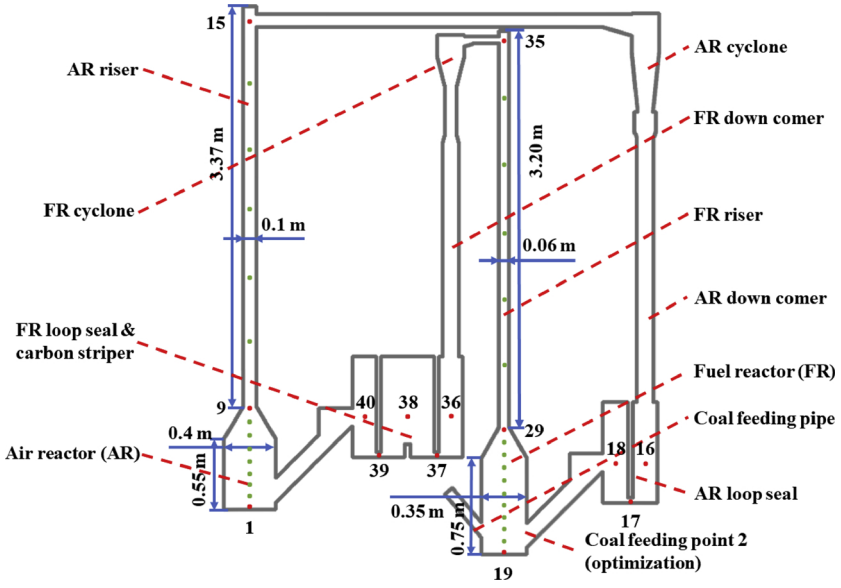

Fig. 1. Structure of the 50 kW_{th} CLC reactor.

Table 4
Proximate and ultimate analysis of coal used in experiment and simulation.

Proximate analysis (ad wt.%)			
Fix carbon	48.46	Volatiles	15.54
Moisture	1.66	Ash	34.34
Ultimate analysis (ad wt.%)			
C	55.26	H	2.12
O	5.39	N	0.79
S	0.44		

gas volume fraction is in dry basis, and N_2 is not considered in calculation. As it is shown in Table 6, slight difference can be observed between the results of simulation and experiment. Nevertheless, it is quite obvious that in these cases, the simulation results conform with the experiment measurements in a relatively reasonable tendency and the difference among results are acceptable for such a complex system with the mutual influencing factors from lots of aspects. In addition, to analyze the hydrodynamics in the unit, especially in the FR, the pressure profile in FR was investigated and the results are shown in Fig. 2. Superficial velocity, which affects the bed inventory as well as pressure distribution was adopted as the regulation parameter. As it can be seen in Fig. 2, the results measured by the two pressure detecting points in FR during experiment are adopted and these results disperse nearly around the lines of simulation results. And the data shows nearly the same evolution tendency in both cases. All in all, based on the validations shown above relating to the chemical reaction and hydrodynamics in the system, the works on the simulation of 50 kW_{th} CLC reactor can reflect the operation in a relatively accurate way and predict the behavior of it.

In the simulation of the CLC reactor, fluid dynamics and reaction details are key points for evaluating the performance of the reactor. Therefore, systematic analyses on these aspects in solid-gas flow were conducted step by step. Firstly, the flow pattern of the solid phase was investigated, especially for the proofs on stable operation and self-adjustment of the reactor. Because as the unit turns into regular and stable state gradually, bed inventory and solid circulation rate in each part are time-dependent and the evolution process can reflect the stability and self-adjustment of the dual circulating fluidized bed reactor. Additionally, due to the pressure difference between the AR and FR, the pressure balance in reactor, especially in loop seal, plays a crucial role in maintaining stable operation and gas isolation. Therefore, the pressure balance was investigated. Furthermore, the residence time of OC and char in FR are crucial because the char gasification process in fluidized bed is usually the rate-limiting step among all reactions happening in a CLC unit. As OC and char mix uniformly and char particles flow out of FR with the entrainment of OC, investigation on their residence time can help to make a deep analysis of the gas-solid reactive flow in FR. Then, the flow pattern of the gas phase was studied. Based on the results, details of the movement trail of coal in FR, products of coal pyrolysis as well as coal char gasification can be provided. Finally, some issues that should be optimized were found during the simulation, like the short residence time of char and the bad diffusion and mixture

Table 6
The validation of the model about FR exhausts components.

Cases	U_{FR} (m/s)	T (K)	H_2O ratio (%)	CO_2 (%) sim/exp	CO (%) sim/exp	CH_4 (%) sim/exp	H_2 (%) sim/exp
Case 1	0.3	1223	50	83.6/84.8	9.5/8.2	6.2/7.0	0.7/0
Case 2	0.3	1273	50	94.1/92.5	3.9/5.5	1.6/2.0	0.4/0
Case 3	0.3	1173	25	76.7/78.1	17.0/15.3	5.2/6.4	1.1/0.2
Case 4	0.3	1173	75	79.1/75.5	13.1/13.7	3.3/4.9	4.5/5.9
Case 5	0.2	1173	50	78.7/78.3	14.9/15.4	3.8/4.6	2.6/1.7
Case 6	0.4	1173	50	70.2/73.5	20.0/18.8	5.7/4.6	4.1/3.1

Note: Case 2 is the main condition in this work, others are for validation.

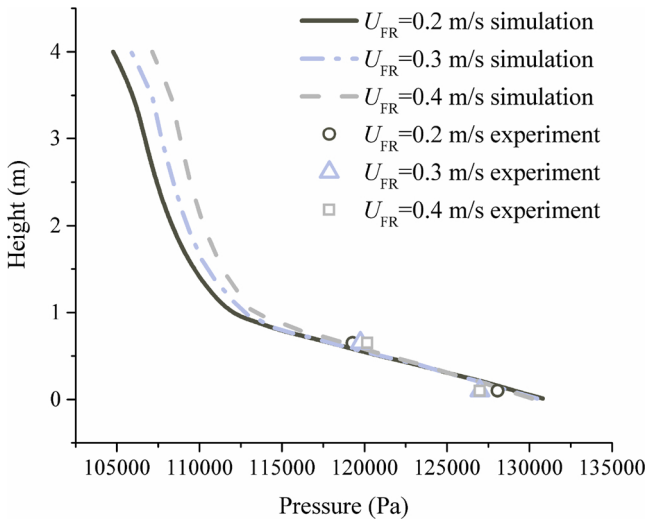

Fig. 2. Experimental measurements *vs.* simulation results of the pressure profile in FR.

of volatile with OC. Accordingly, optimization of the FR configuration were further conducted to achieve better performance of the reactor.

4.2. Flow patterns of solid phase

Fig. 3 shows the typical contours of the instantaneous solid volume fraction distribution of OC at different time from the beginning to the fully-fluidized state. At 0 s, OC particles are accumulated at the bottom of the AR, FR and loop seal, with the initial solid volume fraction of 0.625. At 3 s, OC in FR flows out and is entrained into the riser unsteadily. OC in the loop seal of FR recycles back into the AR and the height of OC in the middle and right chamber of FR loop seal decline as the OC accumulating in the inclined tube. When the simulation reaches 25 s, OC in the AR flows into the riser and the middle chamber of FR loop seal operates like a waterfall. At 70 s, the fluidization state of OC reaches the steady state. At this time, the solid circulation rate of OC is 1.7 kg/s, agreeing well with the design parameter. Fig. 4 shows the

Table 5
Initial and boundary conditions.

Initial condition			
AR initial bed inventory (kg)	88.0	FR initial bed inventory (kg)	143.5
Down comer initial bed inventory (including the part of supply chamber) (kg)	73.8/84.5	Pressure (Pa)	101325
Particle closely-packed volume fraction	0.625	Temperature (K)	1273

Boundary condition			
$P_{FR/AR\ outlet}$ (Pa)	101325	$U_{recycle}$ (m/s, FR/AR)	0.144 (N_2+H_2O/N_2)
U_{supply} (m/s, FR/AR)	0.054 (N_2+H_2O/N_2)	$U_{carbon\ striper}$ (m/s)	0.072 (N_2+H_2O)
U_{AR} (m/s)	0.585 (Air)	U_{FR} (m/s)	0.3 (N2 + H2O)
H_2O ratio (vol.%)	50	Coal feeding (kg/h)	7.3

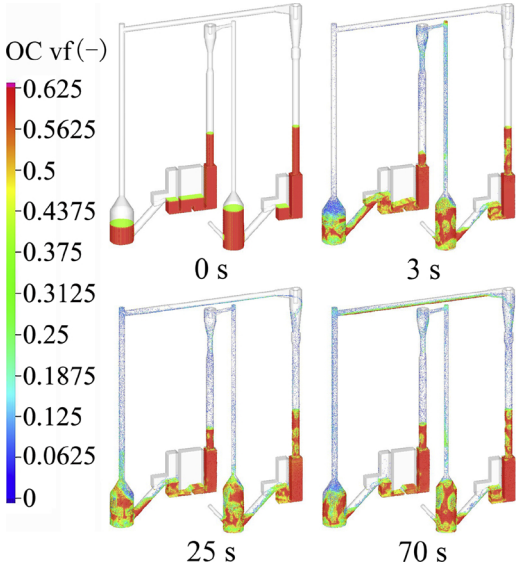

Fig. 3. Instantaneous solid volume fraction distributions.

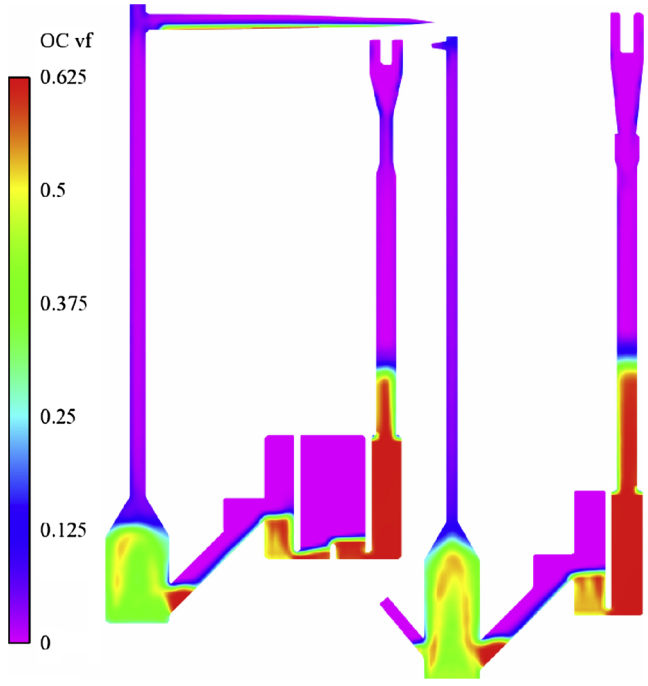

Fig. 4. Time-averaged (30–70 s) solid volume fraction profile under steady state.

time-averaged solid volume fraction of the OC at steady state, which indicates the typical flow pattern in FR and AR. The solid volume fraction in FR is higher than that in AR, because FR is in the bubbling region whereas AR is in the turbulent region. The distribution of OC in AR and FR increase first and then reduce from the center of reactor to the wall because OC particles in the center of reactor are entrained by the drag force, flowing upwards and sideways.

4.3. The process of bed material rebalance

As shown in Fig. 3, it can be found that the OC distribution rebalances at steady state and is different from that at 0 s. Factually, the initial arrangement of OC is based on the experience of design and experimental results, and the distribution of OC within 0–70 s is under dynamic balance. This phenomenon, which can be obviously observed

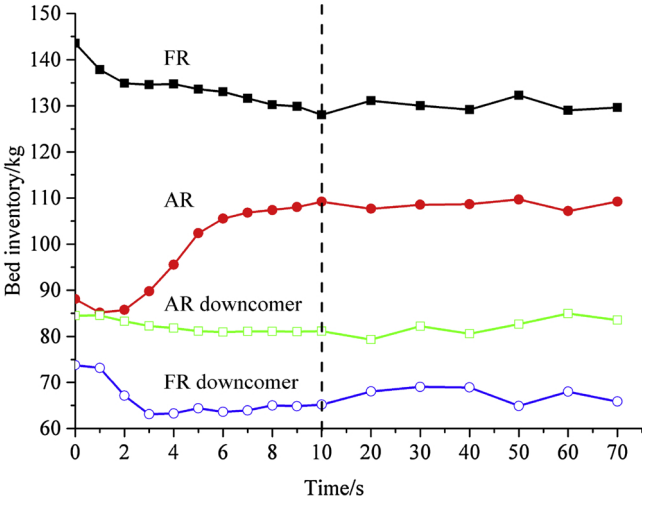

Fig. 5. Self-adjustment of bed inventory in each part of the unit.

from the bed inventory height in down comer, indicates self-adjustment ability of bed inventory and operation stability in the whole unit. Fig. 5 shows the self-adjustment process of bed inventory of AR, FR, AR down comer, and FR down comer in the simulation. Note that, the one in down comer includes OC in supply chamber. It is explicit that the simulation results can be divided into two parts: the first one is 0–10 s and the second one is 10–70 s. From 0 s to 10 s, the bed inventory in each part changes gradually with different tendency and this is the main process of OC rebalance. From 10 s to 70 s, bed inventory keeps dynamic balance with slight fluctuation. In this process, self-adjustment still exists, leading to the fluctuation of bed inventory. The reason of OC rebalance can be explained that the solid circulation rate and pressure in AR and FR reach balance gradually, and the mass of OC in each part redistributes accordingly to achieve a pressure balance, regulating and keeping normal circulation in the reactor.

Fig. 6 shows the typical evolution process of solid circulation rate in the simulation. The process of bed inventory self-adjustment is affected by solid circulation rate, which is a critical parameter in reactor operation. During the operation, solid circulation rate will affect the OC residence time, while the OC residence time is the main factor to influence the char residence time in FR because of mixing and entrainment. Solid circulation rate is also a time-dependent variable, and the difference between solid circulation rate at inlet and outlet of AR and FR will lead to the change of bed inventory, which eventually affects

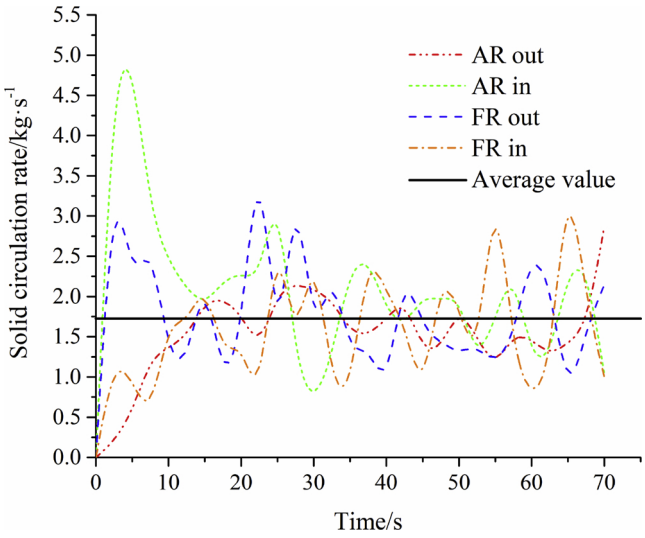

Fig. 6. Evolution of solid circulation rate at the inlet and outlet of AR and FR.

solid circulation in return. As shown in Fig. 6, the solid circulation rate at the inlet and outlet of AR and FR change sharply at first, especially the one at the inlet of AR. After 10 s, the solid circulation rate of each part reaches dynamic balance and fluctuates around the average value.

4.4. Pressure balance

Pressure balance can affect the particle fluidization, like bed inventory and OC circulation. On the other side, the specific initial OC arrangement as well as the operational conditions will determine the pressure balance in turn. In order to comprehensively study the pressure balance of the unit, several pressure detecting points were set in AR, FR and riser, and the arrangement of the detection points is listed in Fig. 1. Points 1–9, 10–15, 16–18, 19–29, 30–35, and 36–40 are in AR, AR raiser, AR loop seal, FR, FR raiser, and FR loop seal, respectively. Every point in each part of the reactor connects to one another sequentially in turn and each part is also connected in sequence as "AR - AR raiser - AR loop seal - FR - FR raiser - FR loop seal - AR". As can be seen in Fig. 7, the pressure drop in AR and FR expansion section is 9669 Pa and 15,710 Pa, respectively, which depends on the bed inventory in AR and FR. The pressure gradient of FR is higher than that of AR and the pressure gradient of FR riser is higher than that of AR riser, indicating the fluidization state of each part. In addition, values of point 16 and 40 in the recycle chamber of loop seal are higher than those of point A and B, which are at the connection of the loop seal and AR, FR. Moreover, pressure of points in recycle chamber (16, 40) and supply chamber (18, 38) are higher than those of points 17, 37 and 39, meaning that the AR loop seal and FR loop seal can overcome the pressure difference between AR and FR, maintaining steady circulation of OC and gas isolation.

4.5. Residence time distribution of OC and char

For a CLC unit with a fluidized bed reactor as FR, some unconverted char flows out of FR with the entrainment of gas and OC, leading to the low carbon capture efficiency. Moreover, there are also some unconverted combustible gases escaping from FR with the break of bubbles, which is also related to the fluidization of char and OC and detrimental to the performance of the CLC unit. In the CPFD simulation, particles are solved in the Lagrangian manner, thus the information of each particle can be obtained. To make a comprehensive understanding on the residence time of these two kinds of particles in FR, the residence time distributions of OC and char were studied in the simulation of the individual FR within enough simulation time, and the results are shown in Fig. 8 and Fig. 9, respectively. It should be noted that the coal and OC particles size in the simulation was considered as normally distributed. From the scatter diagram, the probability density of particles in specific radius or residence time can be obtained in a visualized way. Fig. 8 shows the residence time distribution of char particles at different radius and the frequency distribution under different residence time from the perspective of statistical significance. It is obvious that for different initial radius ranging from 100 μm to 300 μm, char residence time scatters from 1 s to 195 s and the frequency distribution of residence time distributes as exponential type with the maximum on 0–10 s. 80% char particles distribute ranging from 0 s to 70 s, which is not enough for total gasification. Besides, the average residence time of all particles is 37 s, as indicated by the blue dashed line in Fig. 8. However, the effect of char particle radius on the residence time is not conspicuous to some extent because the solid concentration in FR is relatively high and the particle collision covers it up. For the particles with short residence time, they are mainly influenced by the entrainment of fluidization agent, whereas the mixing and entrainment of OC have relatively less effect on it. For some particles, the residence time is long enough for complete conversion, but the amount of these particles is quite few, as demonstrated by the red curve in Fig. 8. The residence time of these char particles is mainly affected by the entrainment of OC, while the fluidization agent has less influence on it. At last, it can be concluded that the residence time of char is too short to be totally converted. Therefore, an optimization to achieve longer residence time should be adopted to improve carbon capture efficiency.

Additionally, the residence time of OC was also investigated and the distribution shows different tendency which is more uniform than that of coal char, as can be seen in Fig. 9. The residence time of OC recycling from FR loop seal is affected by the fluidization agent as well as the entrainment of OC particles that were originally stored in FR. Most of the OC particles scatter in the range of 3 s to 205 s, and the frequency distribution of the residence time distributes with a peak value on 40–50 s. Around 80% OC particles distribute ranging from 20 s to 130 s and the average residence time of the OC particles is 75 s, which is approximate to the value calculated by average bed inventory of FR and solid circulation rate. Because of the particle collision, the effect of particle radius on residence time is not conspicuous as well as observed in Fig. 9.

4.6. Gas distribution in FR

The time-averaged volume fraction distribution profile of H_2, CO, CH_4, CO_2, and H_2O in the middle section of FR is shown in Fig. 10. As coal is introduced into the coal feeding pipe, coal pyrolysis and char gasification happen at the bottom of the coal feeding pipe. Then, the volatile matters release from coal flowing upwards in plume. And the volatile plume, especially CH_4, can reflects the movement trail of coal to some extent, because CH_4 is only from the release of coal volatile in the simulation. The volume fraction of H_2, CO, CH_4, and CO_2 all reach the maximum at the position of the connection between FR and coal feeding pipe, where volatile release and char gasification processes happen. Then, char particles are fluidized in FR, mixing with OC and dispersing to the whole FR. Thus, FR can be divided into two parts: the first one is volatile plume where OC reacts with volatile and char gasification products, and the second one is the rest part of FR where OC only reacts with char gasification products. However, volatile and char flow with the fluidization gas and cannot totally diffuse to the whole FR, which is caused by the one-point coal feeding mode. Although char particles are entrained by the OC, it is still difficult for char particles, which are lighter than OC particles, to diffuse to the whole FR totally. In addition, the one-point coal feeding mode makes the mixing between the pyrolysis products and OC to be not sufficient enough, leading to the low utilization efficiency of the reactor. For the sake of operation optimization, the coal feeding mode should be changed to, *e.g.*, the two oppositely-collocated coal feeding points, so the rest part of FR can be

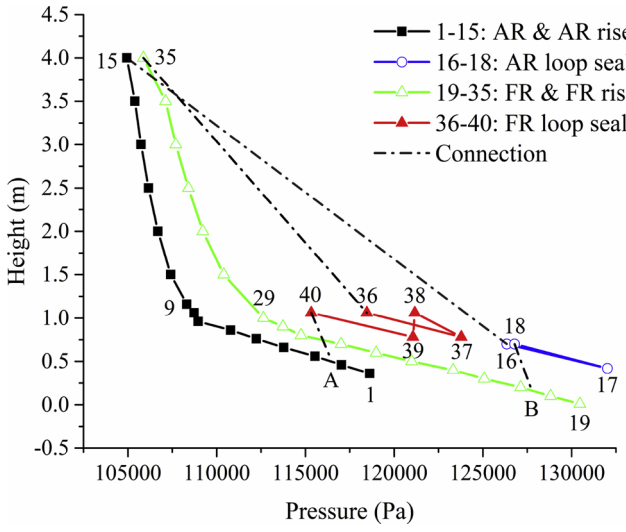

Fig. 7. Time-averaged (30–70 s) pressure profile under steady state.

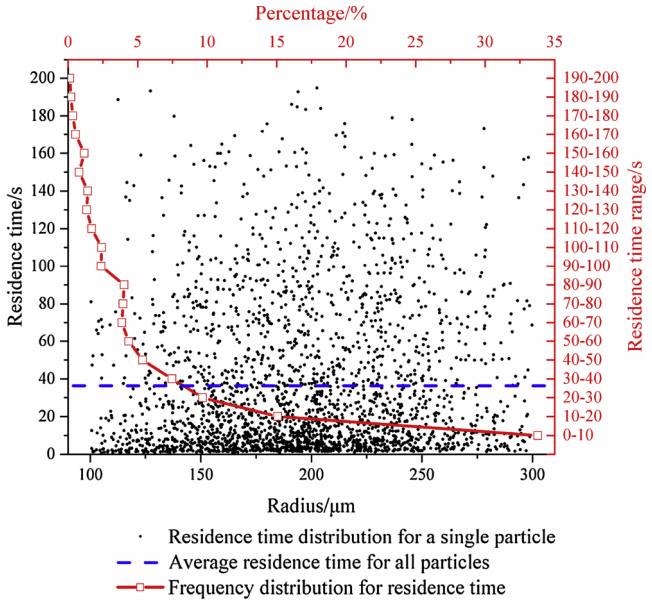

Fig. 8. Residence time distribution of char under different radius and frequency distribution under different residence time ranges.

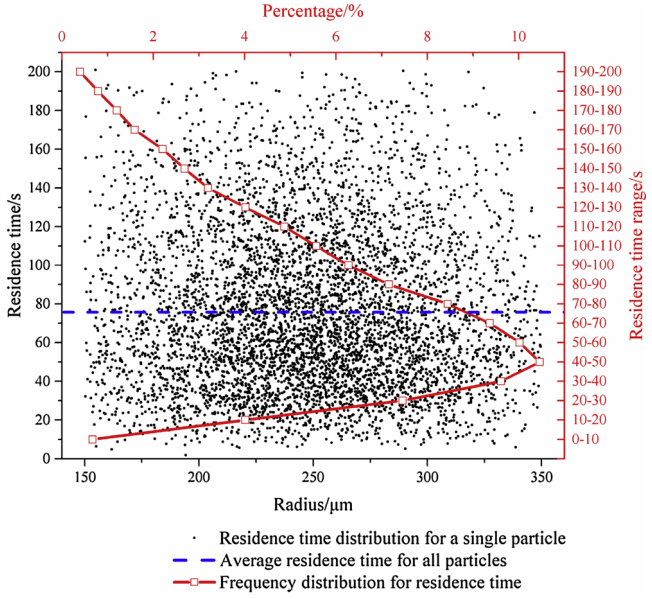

Fig. 9. Residence time distribution of OC under different radius and frequency distribution under different residence time ranges.

utilized and more lattice oxygen will be provided to the conversion of volatiles. In addition, H_2O distribution is influenced by the structure of FR and the inclined pipe between FR and AR loop seal makes H_2O flow to the left side.

4.7. Operation optimization

As can be concluded from the simulation results, there are at least two places in this reactor that need to be optimized. The first one is the nonuniform mixing between combustible gases in volatile plume and OC, and the second one is the relatively short residence time of char particles in FR. To solve the first problem, the two oppositely-collocated coal feeding points can be adopted. And for the second one, the height of FR should be increased to lengthen the char residence time, as well as to extend the reaction path for all reactions in FR.

4.7.1. Optimization of the coal feeding mode

The one-point coal feeding mode cannot guarantee the coal pyrolysis products to diffuse throughout the whole FR, leading to low utilization efficiency of the reactor. Hence, two oppositely-collocated coal feeding points are adopted in this part to optimize the operation and half of the coal is fed at the new point as shown in Fig. 1. Additionally, it is also possible that coal particle can be introduced into the recycle chamber of AR loop seal and coal particles can flow with OC, entering FR at the point similar to the one in this work. Fig. 11 shows the time-averaged volume fraction distribution profiles of H_2, CO, CH_4, CO_2, and H_2O. When comparing the results shown in Figs. 10 and 11, it is obvious that the rest of FR can be utilized and the OC in this region can contact and react with the combustible gases in volatile plume. H_2, CO, CH_4, and CO_2 reach the maximum values after the coal is introduced from the coal feeding points for a period of time, during which coal particles pyrolyze quickly into char and volatiles. Whereas, the concentrations of combustible gas products at the connection between FR and coal feeding pipe are higher than these at the new coal feeding point, indicating that the new coal feeding pipe perform better than the old one. Besides, CO_2 concentration at the old coal feeding point is higher than the new one because the fluidization agent flows towards left under the influence of FR structure. Fig. 12 compares the FR exhausts gas volume fraction of the two kinds of coal feeding mode. It shows that the opposite-collocated coal feeding mode has positive effect on the operation, which is better than the old one with only one coal feeding point. CO_2 in the exhausts increases from 94.15% to 96.37%. CO, CH_4 and H_2 decreases from 3.90% to 2.27%, from 1.85% to 1.08% and from 0.37% to 0.25%, respectively. Therefore, more coal char can be converted in FR with the new coal feeding mode. The better results can be explained by the better contact between OC and char particles. Also, it is expected that the two oppositely-collocated coal feeding mode will achieve better performance under lower operational temperature.

4.7.2. Optimization of FR structure

As discussed in Section 4.5, the residence time of char particle in FR is relatively short that it cannot be fully consumed, which is not beneficial for fuel conversion and carbon capture. As an optimization, a higher FR configuration with more bed inventory is proposed to lengthen char residence time by the effect of mixing and entrainment between OC and char. Additionally, as a higher FR can enhance the gas-solid contact between OC and combustible gases, the reaction path of both char and combustible gases can be extended. The optimization structure which is double of original FR height was simulated with one/two coal feeding points, where the FR inlet velocity and H_2O concentration in fluidizing agent were not changed. Moreover, additional secondary air of 4 L/s was introduced at the connection section of the FR and riser in this case to stabilize OC circulation. As can be seen in Fig. 13, the char residence time scatters from 1 s to 385 s and the frequency distribution of residence time is different with the original case. More particles distribute with longer residence time in the graph and 80% particles distribute ranging from 0 s to 220 s, which is wider than the one before optimization (0–70 s). Besides, the average residence time of all char particles before optimization is 37 s, but it is 112 s with a higher FR, as indicated by the blue dashed line in Fig. 13. Therefore, the residence time of char in FR is quite improved and better performance of the CLC unit is achieved. Fig. 14 compares the FR exhausts gas volume fraction under different FR heights and coal feeding modes. It shows that the higher FR with opposite-collocated coal feeding mode is better than the old one with only one coal feeding point and lower FR. CO_2 volume fraction in the exhausts increases to 99.1 vol.%. Therefore, more coal char and combustible gases in the volatile can be converted in FR, leading to the decrease of combustible gases in the FR exhausts.

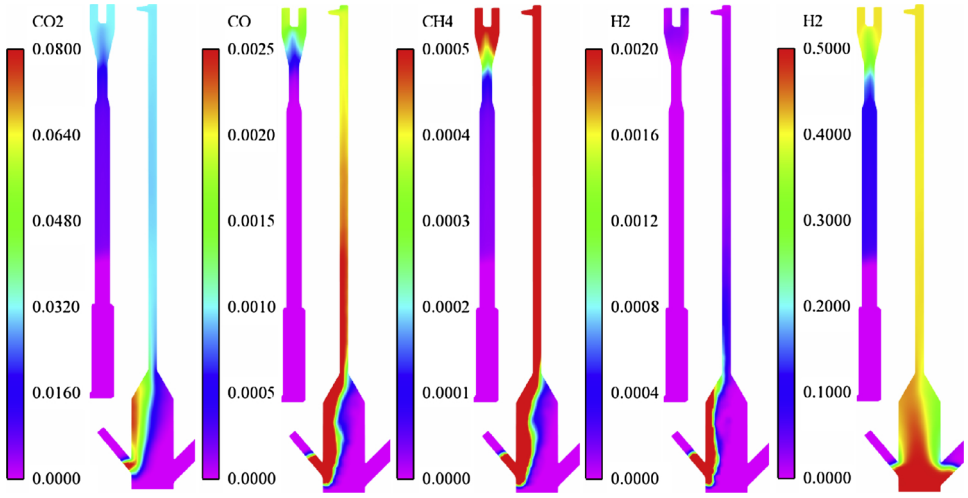

Fig. 10. Time-averaged (30–70 s) gas volume fraction profiles in FR under steady state.

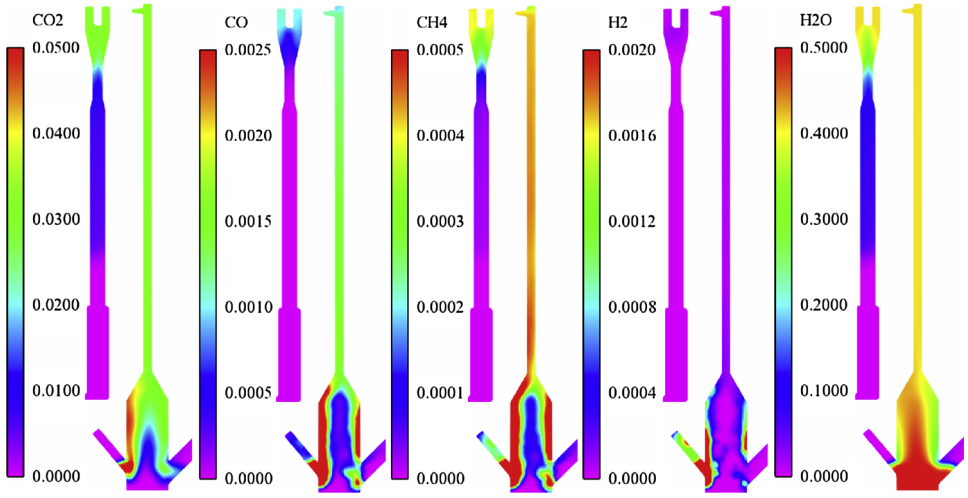

Fig. 11. Time-averaged (30–70 s) gas volume fraction profiles in FR under steady state employing optimal coal feeding mode.

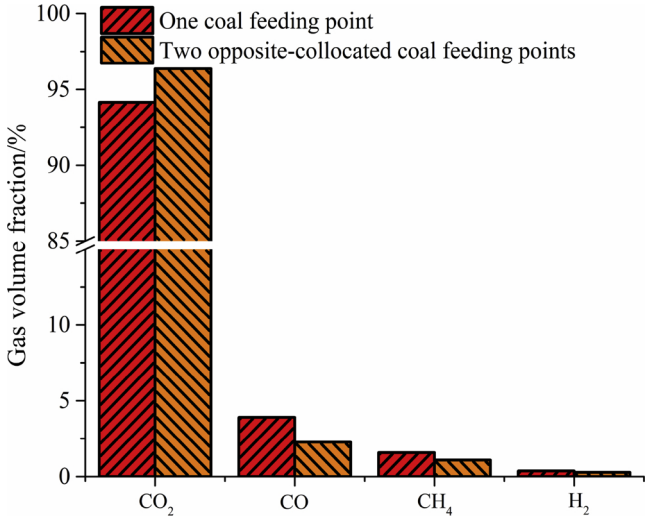

Fig. 12. Results of the FR exhausts gas volume fraction under different coal feeding modes.

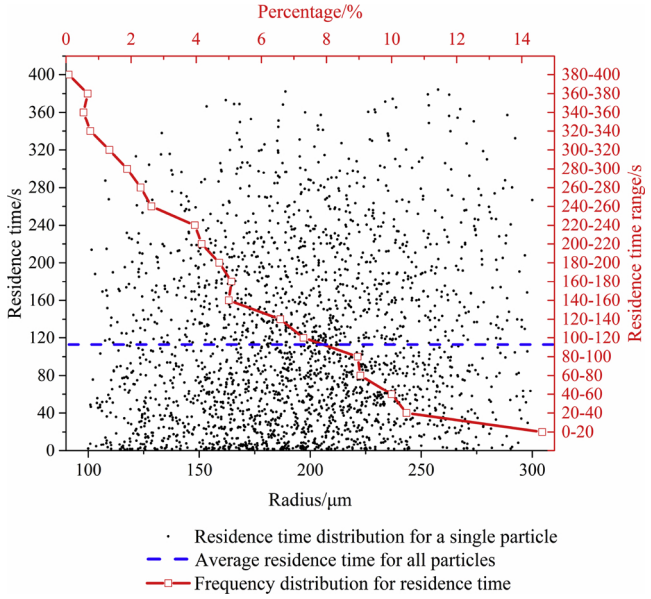

Fig. 13. Residence time distribution of char under different radius and frequency distribution under different residence time ranges (after optimization).

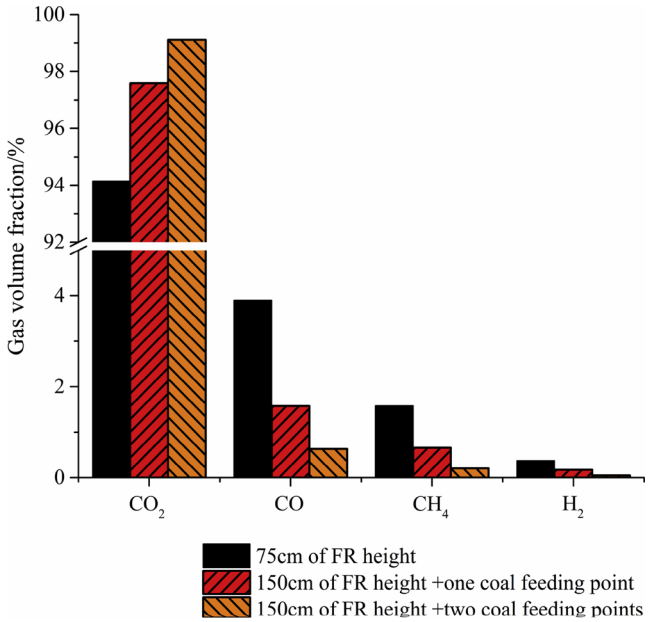

Fig. 14. FR exhausts gas volume fractions under different FR heights and coal feeding modes.

5. Conclusions

In this work, a three-dimension CPFD simulation was conducted for a full-scale 50 kW_{th} coal-fueled dual circulating fluidized bed reactor of CLC. CPFD simulation was proved to be an effective and economic way for the rational design and optimization of the CLC unit. According to the simulation results, the fluidization characteristics of gas-solid reactive flow as well as reactor optimization like coal feeding mode and FR height were investigated. The main conclusions can be drawn as below:

- The simulation results agreed well with experimental measurements and the CPFD simulation can provided critical details of the chemical reactions and gas-solid hydrodynamics involved in the CLC reactor, which were of great significance for the optimization and operation of the CLC unit.
- A systematic study on the fluidization characteristics in the CLC unit was conducted. Based on the evolution trend of bed inventory and solid circulation rate, self-adjustment ability was observed in the whole reactor to reach the balance state of OC and pressure distribution. In addition, loop seal played a critical role in OC rebalance with good gas isolation.
- The residence time distribution of OC and char was also investigated. It was found that the residence time of char particles was too short to be completely consumed. The residence time of 80% char particles distributed between 0–70 s. To increase the residence time of char so as to extend reaction path, a higher FR configuration was proposed as an optimization.
- Under the condition of one coal feeding point, the combustible gases in volatile cannot disperse to the whole FR, therefore the FR was not utilized efficiently. The two oppositely-collocated coal feeding mode was adopted as an optimization and it was proved to have positive impact on the operation. CO_2 in the exhausts was increased and the concentrations of combustible gases were decreased accordingly.

Acknowledgements

This work was presented and benefited from discussions at the “5th International Conference on Chemical Looping” (Park City, UT, USA, 2018). The authors acknowledge the support from the “National Key R &D Program of China (2018YFB0605403)”.

References

Abad, A., Adanez, J., Garcia-Labiano, F., et al., 2007. Mapping of the range of operational conditions for Cu-, Fe-, and Ni-based oxygen carriers in chemical-looping combustion. Chem. Eng. Sci. 62, 533–549.
Abad, A., Mattisson, T., Lyngfelt, A., 2006. Chemical-looping combustion in a 300 W continuously operating reactor system using a manganese-based oxygen carrier. Fuel 85, 1174–1185.
Adanez, J., Abad, A., Garcia-Labiano, F., et al., 2012. Progress in chemical-looping combustion and reforming technologies. Prog. Energy Combust. Sci. 38, 215–282.
Andrews, M.J., O'Rourke, P.J., 1996. The multiphase particle-in-cell (MP-PIC) method for dense particulate flows. Int. J. Multiphas. Flow 22, 379–402.
Breault, R.W., Monazam, E.R., 2016. Modeling of the reduction of hematite in the chemical looping combustion of methane using Barracuda. Energy Technol-GER. 4, 1221–1229.
Breault, R.W., Weber, J., Straub, D., 2017. Computational Fluid Dynamics modeling of the fuel reactor in NETL's 50 kW_{th} chemical looping facility. J. Energy Resour-ASME 139, 1–8.
Bustamante, et al., 2004. Kinetics of the homogeneous reverse water–gas shift reaction at high temperature. AIChE J. 50 (5), 1028–1041.
Bustamante, et al., 2005. Uncatalyzed and wall-catalyzed forward water–gas shift reaction kinetics. AIChE J. 51 (5), 1440–1454.
Deng, Z., Xiao, R., Jin, B., et al., 2008. Multiphase CFD modeling for a chemical looping combustion process (fuel reactor). Powder Technol. 31, 1754–1766.
Deng, Z., Xiao, R., Jin, B., Song, Q., 2009. Numerical simulation of chemical looping combustion process with $CaSO_4$ oxygen carrier. Int. J. Greenh. Gas Control 3, 368–375.
Fan, L.–S., Li, F., 2010. Chemical looping technology and its fossil energy conversion applications. Ind. Eng. Chem. Res. 49, 10200–10211.
Guan, Y., Chang, J., Zhang, K., 2014. Three-dimensional CFD simulation of hydrodynamics in an interconnected fluidized bed for chemical looping combustion. Powder Technol. 268, 316–328.
Hamilton, M., Whitty, K., Lighty, J.A., 2016. Incorporating oxygen uncoupling kinetics into Computational Fluid Dynamic simulations of a chemical looping system. Energy Technol-GER. 4, 1237–1246.
Jung, J., Gamwo, I.K., 2008. Multiphase CFD-based models for chemical looping combustion process: fuel reactor modeling. Powder Technol. 183, 401–409.
Leion, H., Mattisson, T., Lyngfelt, A., 2008. Solid fuels in chemical-looping combustion. Int. J. Greenh. Gas Control 2, 180–193.
Linderholm, C., Abad, A., Mattisson, T., Lyngfelt, A., 2008. 160 h of chemical-looping combustion in a 10 kW reactor system with a NiO-based oxygen carrier. Int. J. Greenh. Gas Control 2, 520–530.
Lyngfelt, A., Leckner, B., 2015. A 1000MW_{th} boiler for chemical-looping combustion of solid fuels-Discussion of design and costs. ACS Appl. Energy Mater. 157, 475–487.
Lyngfelt, A., Lecknor, B., Mattisson, T., 2001. A fluidized bed combustion process with inherent CO_2 separation: an application of chemical looping combustion. Chem. Eng. Sci. 56, 3101–3113.
Ma, J., Tian, X., Zhao, H., et al., 2018. Performance of a 50 kW_{th} coal-fuelled chemical looping combustor. Int. J. Greenh. Gas Control 75, 98–106.
Mattisson, T., Lyngfelt, A., Cho, P., 2001. The use of iron oxide as an oxygen carrier in chemical-looping combustion of methane with inherent separation of CO_2. Fuel 80, 1953–1962.
Mahalatkar, K., Kuhlman, J., Huckaby, E.D., 2011a. Computational fluid dynamic simulations of chemical looping fuel reactors utilizing gaseous fuels. Chem. Eng. Sci. 66, 469–479.
Mahalatkar, K., Kuhlman, J., Huckaby, E.D., 2011b. Simulations of a circulating fluidized bed chemical looping combustion system utilizing gaseous fuel. Oil Gas Sci. Technol. 66, 301–311.
Mahalatkar, K., Kuhlman, J., Huckaby, E.D., 2011c. CFD simulation of a chemical-looping fuel reactor utilizing solid fuel. Chem. Eng. Sci. 66, 3617–3627.
Metz, B., Davidson, O., de Coninck, H., et al., 2005. IPCC Special Report on Carbon Capture and Storage. Intergovernmental Panel on Climate Change. Working Group III.
Nandy, A., Loha, C., Gu, S., et al., 2016. Present status and overview of chemical looping combustion technology. Renew. Sust. Energy Rev. 59, 597–619.
Parker, J.M., 2014. CFD model for the simulation of chemical looping combustion. Powder Technol. 265, 47–53.
Shao, Y., Zhang, Y., Wang, X., et al., 2017. Three dimensional full loop modeling and optimization of an in situ gasification chemical looping combustion system. Energy Fuel. 31, 13859–13870.
Snider, D.M., 2001. An incompressible three-dimensional multiphase particle-in-cell model for dense particle flows. J. Comput. Phys. 170, 523–549.
Snider, D.M., Clark, S.M., O'Rourke, P.J., 2011. Eulerian–Lagrangian method for three-dimensional thermal reacting flow with application to coal gasifiers. Chem. Eng. Sci. 66, 1285–1295.
Son, S.R., Kim, S.D., 2006. Chemical-looping combustion with NiO and Fe2O3 in a thermobalance and circulating fluidized bed reactor with double loops. Ind. Eng. Chem. Res. 45, 2689–2696.
Su, M., Zhao, H., 2016. Modifying the inter-phase drag via solid volume fraction gradient for CFD simulation of fast fluidized beds. AIChE J. 63, 2588–2598.
Su, M., Zhao, H., Ma, J., 2015. Computational fluid dynamics simulation for chemical

looping combustion of coal in a dual circulation fluidized bed. Energy Convers. Manage. 105, 1–12.
Syamlal, M., Bissett, L.A., 1992. METC Gasifier Advanced Simulation (MGAS) Model. DOE/METC-92/4108, DE92 001111.
Tabib, M.V., Johansen, S.T., Amini, S., 2013. A 3D CFD-DEM methodology for simulating industrial scale packed bed chemical looping combustion reactors. Ind. Eng. Chem. Res. 52, 12041–12058.
Wang, S., Lu, H., Zhao, F., et al., 2014. CFD studies of dual circulating fluidized bed reactors for chemical looping combustion processes. Chem. Eng. J. 236, 121–130.
Wang, S., Yang, Y., Lu, H., et al., 2011. Hydrodynamic simulation of fuel reactor in chemical looping combustion process. Chem. Eng. Res. Des. 89, 1501–1510.
Wang, X., Jin, B., Zhang, Y., et al., 2013. Three dimensional modeling of a coal-fired chemical looping combustion process in the circulating fluidized bed fuel reactor. Energ. Fuel. 27, 2173–2184.
Zhang, Z., Zhou, L., Agarwal, R., 2014. Transient simulations of spouted fluidized bed for coal-direct chemical looping combustion. Energy Fuel. 28, 1548–1560.
Zhao, H., Liu, L., Wang, B., et al., 2008. Sol-gel-derived NiO/$NiAl_2O_4$ oxygen carriers for chemical-looping combustion by coal char. Energy Fuel 22, 898–905.